SUPPLEMENTARY INFORMATION

Nano-optical imaging of exciton-plasmon polaritons in WSe$_2$/Au heterostructures

Raghunandan B. Iyer[1,2], Yilong Luan[1,3], Ruth Shinar[2]*, Joseph Shinar[1,2,3]*, Zhe Fei[1,3]*

[1]Ames Laboratory, U. S. Department of Energy, Iowa State University, Ames, Iowa 50011, USA
[2]Department of Electrical & Computer Engineering, Iowa State University, Ames, Iowa 50011, USA
[3]Department of Physics and Astronomy, Iowa State University, Ames, Iowa 50011, USA

*Correspondence: (R.S.) rshinar@iastate.edu; (J.S.) jshinar@iastate.edu; (Z.F.) zfei@iastate.edu

List of Contents

1. Additional information about the experimental setup

To perform a nano-optical imaging study of exciton-plasmon polaritons (EPPs), we employed a scattering-type near-field optical microscope (s-SNOM) from Neaspec GmbH. The setup is built based on a tapping-mode atomic force microscope (AFM). The tips used in the s-SNOM are Pt/Ir-coated silicon tips from nanoandmore.com. The tapping frequency of the tip is set to be ~270 kHz, and the tapping amplitude is about 50 nm. For optical excitations, we used a tunable Ti:sapphire laser (Spectral physics, Tsunami), which covers a spectral range from 1.3 eV to 1.8 eV. The laser is set to be p-polarized to excite transverse-magnetic modes in the samples. The system employs a pseudo-heterodyne interferometric detection method to extract the amplitude (s) and phase (ψ) parts of the near-filed scattering signal. We discuss mainly the amplitude part of the signal, which is sufficient for the extraction of polariton wavelengths. The heterostructure samples were obtained by the mechanical exfoliation of WSe$_2$ bulk crystals onto the gold (Au) thin films. These Au thin films with thicknesses of 50-100 nm were coated on Si wafers before WSe$_2$ exfoliation. All s-SNOM imaging experiments were performed at ambient conditions.

2. Dispersion calculation

In Fig. 2c of the main text, we plot the dispersion diagrams of EPPs of WSe_2 on Au, where the data points obtained from s-SNOM experiments and Comsol simulations are overlaid on the theoretical dispersion colormaps. In the dispersion colormaps, we plot the calculated imaginary part of the p-polarization reflection coefficient $Im(r_p)$. To calculate $Im(r_p)$, we used the transfer matrix method and considered the entire WSe_2/Au/Si multilayer structure. The optical constants of WSe_2 are adopted from previous literature (see Ref. 27 in the main text). The bright curves shown in the dispersion colormaps correspond to transverse magnetic (TM) photonic, plasmonic or polaritonic modes. The dispersion calculation method has been widely applied in the studies of other polaritonic modes including surface plasmon polaritons in graphene, hyperbolic phonon polariton in hexagonal boron nitride, and exciton polaritons in transition-metal dichalcogenide (see Refs. 20 and 21 in the main text).

3. Additional experimental and simulation data

In Fig. S1a and Fig. S2a, we present near-field amplitude images of two additional WSe_2/Au heterostructure samples, where we can see the interference fringes of the EPP modes. The WSe_2 thicknesses are 51 nm and 35 nm, respectively. By analyzing the EPP fringe profiles with Fourier transform (FT), we were able to extract the EPP wavelengths at various excitation energies. We then constructed the dispersion diagrams of the EPP modes of the two samples, which show good consistency with calculated dispersion colormaps (see Fig. S1c and Fig. S2c).

From Fig. 1 of the main text, one can also see bright fringes on the Au substrate, which are generated due to the interference of surface plasmon polaritons (SPPs) at the air/Au interface. In Fig. S3a and Fig. S3b, we plot the fringe profiles on Au extracted from Fig. 1 in the main text and the corresponding FT profiles. We then determine the wavelength of SPPs with $1/\rho = 1/\lambda_p + \cos\alpha/\lambda_0$. Note that the '+ sign' in this equation is different from Eq. 1 in the main text. This is due to the different interference geometry. In the case of EPP mode on WSe_2/Au, the scattering edge is on the left side. In the case of SPP mode on bare Au, the scattering edge is on the right side. With the extracted SPP wavelength at various excitation energies, we were able to construct the dispersion diagram of SPPs at the air/Au interface (see Fig. S3c), which is consistent with the theoretical calculation (colormap).

In Fig. S4, we show the energy-dependent E_z maps of the EPPs obtained from finite-element simulations, based on which we added the simulation data points (triangles) in the dispersion diagram in Fig. 2c of the main text. The finite-element simulations were performed using COMSOL Multiphysics. As sketched in Fig. S4a, EPPs are launched from the left toward the right along the heterostructure sample. Clearly, from Fig. S4b, the EPP wavelength decreases systematically with increasing energy, which is consistent with the dispersion properties of EPPs.

4. Plasmon-exciton coupling

In this section, we add more discussions about the coupling between surface plasmons and excitons, which leads to the generation of EPPs. Fig. S5a is a replot of Fig. 2c in the main text, where the upper and lower branches of EPP modes (marked with blue dashed curves) are revealed. These EPP modes are generated due to the coupling between excitons (marked with an orange dashed line) and SPPs (marked with a green dashed curve). The lower branch of the EPP mode is well-defined, but the upper branch is subject to high damping. In Fig. S5b and Fig. S5c, we plot the dispersion diagrams of the exciton and SPP modes without coupling, respectively. More

specifically, we plot in Fig. S5b the dispersion diagram of a 45-nm-thick WSe$_2$ flake on silicon. Fig. S5c is the dispersion diagram of an artificial WSe$_2$ flake excluding contributions from the A, B, and C excitons. The permittivity of the artificial WSe$_2$ flake is set to be the background contribution ε_{bg}, which is obtained by fitting the experimental permittivity from Beal et al.[1] with Lorentzian oscillators

$$\varepsilon(E) = \varepsilon_{bg} + \sum_{i=A,B,C} \frac{\Omega_i}{E_i^2 - E^2 - iE\Gamma_i}, \qquad [S1]$$

where Ω_i, E_i, Γ_i are the exciton oscillator strength, exciton energy, and exciton linewidth of each exciton. The fitting result is plotted in Fig. S6, which is obtained by using the following parameters are $\varepsilon_{bg} \approx 15$, $E_A = 1.61$ eV, $E_B = 2.16$ eV, $E_C = 2.57$ eV, $\Gamma_A = 0.11$ eV, $\Gamma_B = 0.27$ eV, $\Gamma_C = 0.14$ eV, $\Omega_A = 1.65$ eV^2, $\Omega_B = 1.90$ eV^2, $\Omega_B = 0.45$ eV^2.

Based on the dispersion diagram in Fig. S5, we can estimate the Rabi splitting energy Ω_R (marked with the white arrow) to be about 0.19 eV. The linewidths of A exciton and plasmons close to A exciton energy are $\Gamma_A = 0.11$ eV and $\Gamma_{SPP} = 0.07$ eV, respectively. Therefore, we have $\Omega_R > (\Gamma_A + \Gamma_{SPP})/2$ indicating that excitons are strongly coupled with plasmons.

Such a strong exciton-plasmon coupling is mainly due to the strong confinement of the EPP field inside WSe$_2$, which is sensitively dependent on the thickness of WSe$_2$. As WSe$_2$ thickness increases, more plasmon field is confined inside WSe$_2$, which enables even stronger coupling between excitons and plasmons (see Fig. 4 in the main text). To demonstrate the thickness-dependent plasmon-exciton coupling, we show in Fig. S7 the calculated dispersion diagrams of EPPs with various thicknesses of WSe$_2$. Here, one can see that at small thicknesses (d = 25 nm), the exciton-plasmon coupling is very small and the two branches of EPPs are not clearly separated. As the thickness of WSe$_2$ increases, the coupling strength becomes stronger and the Rabi splitting energy (marked with the white arrow) also increases.

5. Discussions of the lower-k peak

In the main text, we discussed the higher-wavevector (k) peak shown in the Fourier transform (FT) profiles (see Fig. 2b and Fig. 3c in the main text), which is generated due to the interference of two beam paths involving the exciton-plasmon polariton (EPP) mode (see Fig. 1a in the main text). In this section, we wish to discuss the lower-k mode, which is generated by a slightly more complicated interference process involving additional beam paths of the EPP mode.

In Fig. S8, we plot the peak locations of both the lower-k and higher-k peaks extracted from the energy-dependence and thickness-dependence FT profiles. From Fig. S8, we found that the peak location of the lower-k peak is roughly one-half of that of the higher-k peak for both the energy-dependence and thickness-dependence data. This indicates that the fringe period associated with the lower-k peak is two times that of the higher-k peak.

To double-sized period associated with the lower-k peak is generated due to the combination of two types of interferences. As sketched in Fig. S9a, the first type of interference involving beam path 1 (P1) and beam path 2 (P2) is responsible for the higher-k peak as discussed in detail in the main text. The second type of interference is generated by photons from beam path 1 (P1) and beam path 3 (P3). Here in P3, tip-excited EPPs travel to the edge of the sample, reflect back, and then get scattered by the tip into photons. This particular beam path is possible when the in-plane mode is well confined with relatively low losses, so they can be reflected. In our case, the EPP wavelength is about 20-40% of that of free-space photons, so partial reflection at the sample

edge is expected. The period of fringes generated by the second type of interference (ρ_2) is half the size of the EPP wavelength. The period of fringes generated due to the first type of interference (ρ_1) is given by Eq. 1 in the main text. By analyzing our data, we found that ρ_1/ρ_2 is about 5/2 (see Fig. S10). As shown in the simulated interference fringes in Fig. S11, a ratio of $\rho_1/\rho_2 = 5/2$ enables a complicated interference fringe with a long period of $2\rho_1$. We believe this is the origin of the formation of the lower-k peak in the FT profiles.

Supplementary Figures
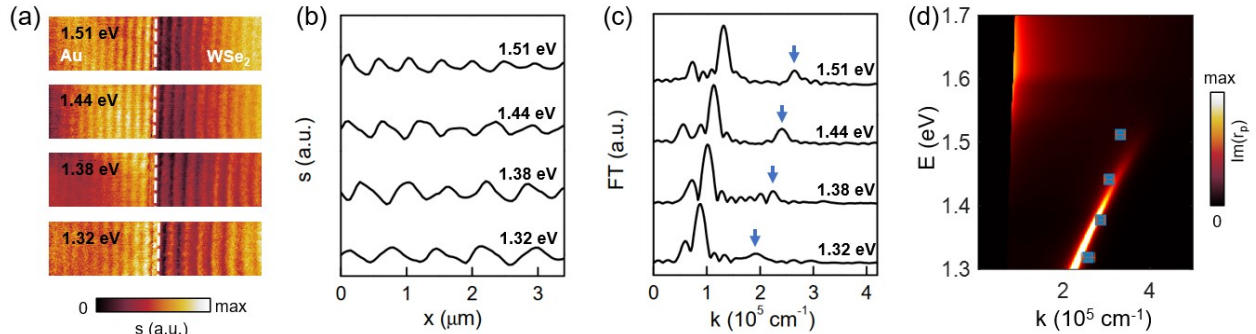
Fig. S1. (a) The near-field amplitude images of a 51-nm-thick WSe_2 flake on an Au film taken with s-SNOM at various laser energies. The white dashed line marks the edge of the WSe_2 flake. (b) (a) Energy-dependent fringe profiles (background subtracted) of WSe_2 extracted from near-field images in panel a. (c) Fourier-transform (FT) of the fringe profiles in panel (b). (d) (c) Dispersion diagrams of EPPs in 51-nm-thick WSe_2 flake on a thin Au film obtained from theoretical calculations (color map) and experimental data (squares). The color map plots the photonic density (DOS) of states.
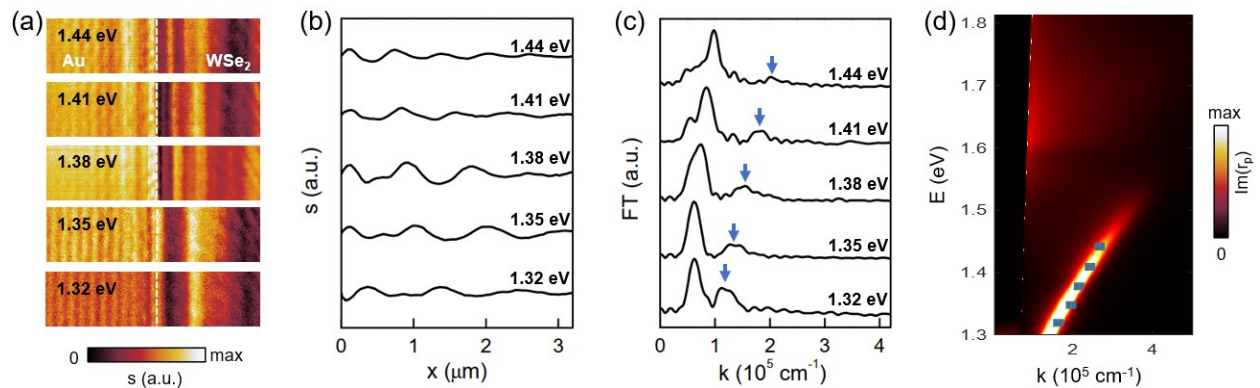

Fig. S2. (a) The near-field amplitude images of a 35-nm-thick WSe_2 flake on an Au film taken at various laser energies. The white dashed lines mark the edge of the WSe_2 flake. (b) Energy-dependent fringe profiles (background subtracted) of WSe_2 extracted from near-field images in panel (a). (c) Fourier-transform (FT) of the fringe profiles in panel (b). (d) Dispersion diagrams of EPPs in 35-nm-thick WSe2 flake on a thin Au film obtained from theoretical calculations (colormap) and experimental data (squares). The colormap plots the photonic density (DOS) of states.
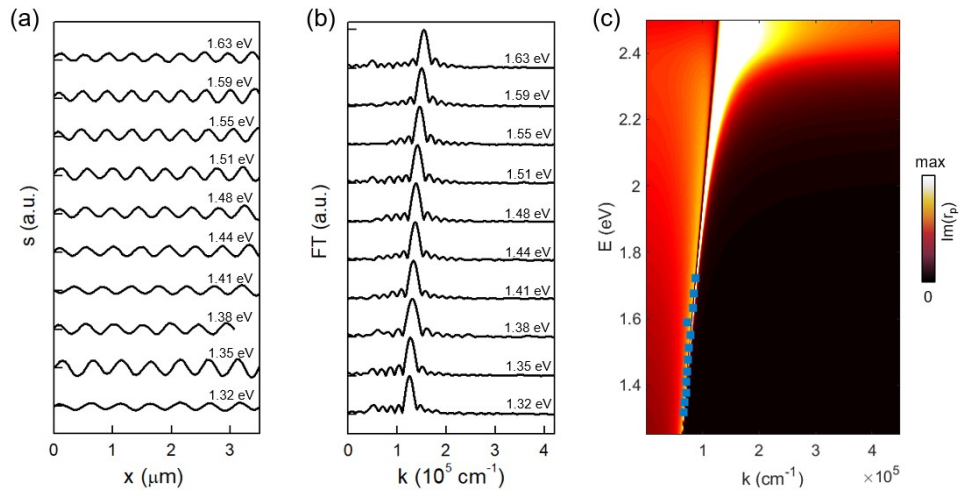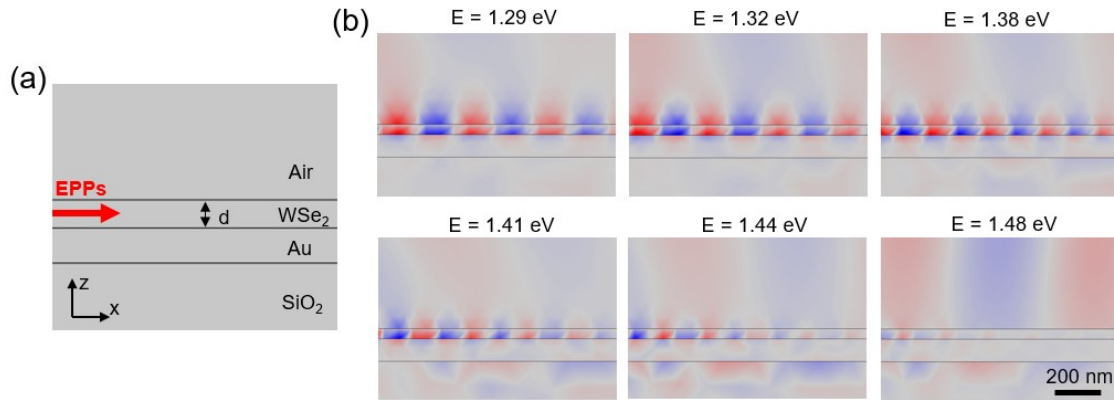
Fig. S3. (a) Line profiles perpendicular to the fringes on Au extracted from Fig. 1 in the main text. (b) Fourier-transform (FT) of the fringe profiles in panel (a). (c) Dispersion diagrams of SPPs on a 100-nm-thick Au film on Si obtained from theoretical calculations (color map) and experimental data (squares). The color map plots the photonic density (DOS) of states.

Fig. S4. (a) Sketch of the air/WSe$_2$/Au/SiO$_2$ four-layer heterostructure model for EPP simulations. (b) The simulated E_z field maps of the EPP mode inside the WSe$_2$/Au heterostructure at various excitation energy. The thickness of WSe$_2$ is $d = 45$ nm.
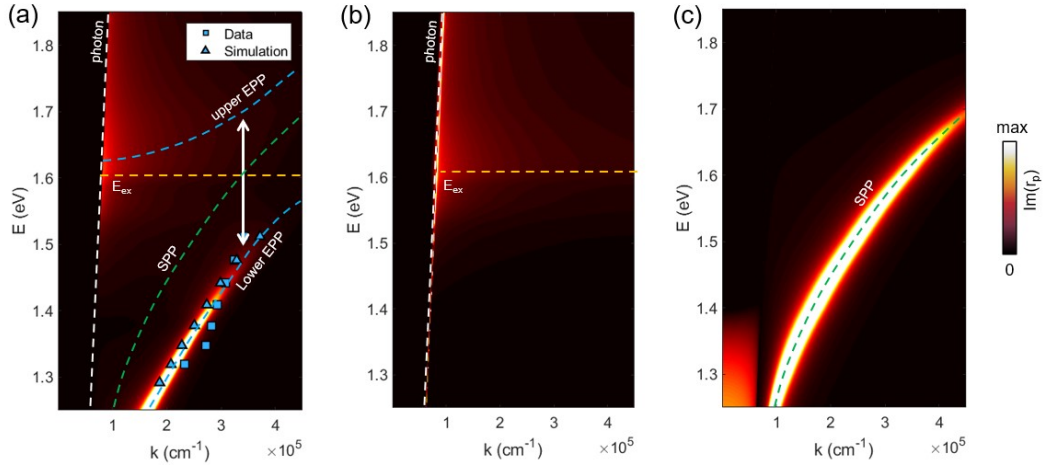
Fig. S5. (a) Dispersion diagram of the EPP mode of a 45-nm-thick WSe$_2$ flake on a 100-nm-thick Au thin film. This is a replot of Fig. 2c in the main text. (b) Dispersion diagram of the A exciton of a bare WSe$_2$ flake on silicon. (c) Dispersion diagram of the SPP mode at the interface of Au and an artificial WSe$_2$ flake without excitons (see discussions in Section 4).
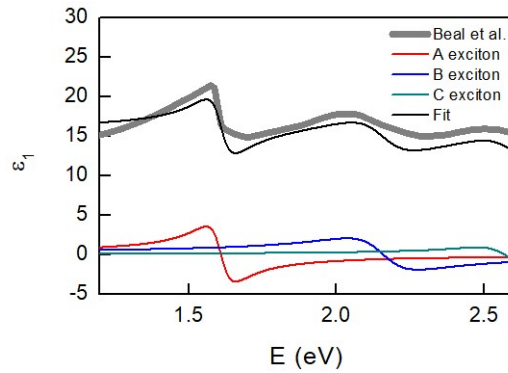

Fig. S6. Fitting of the experimental permittivity of WSe$_2$ adopted from Beal et al. (see Ref. 27 in the main text). The color curves are contributions from individual excitons.
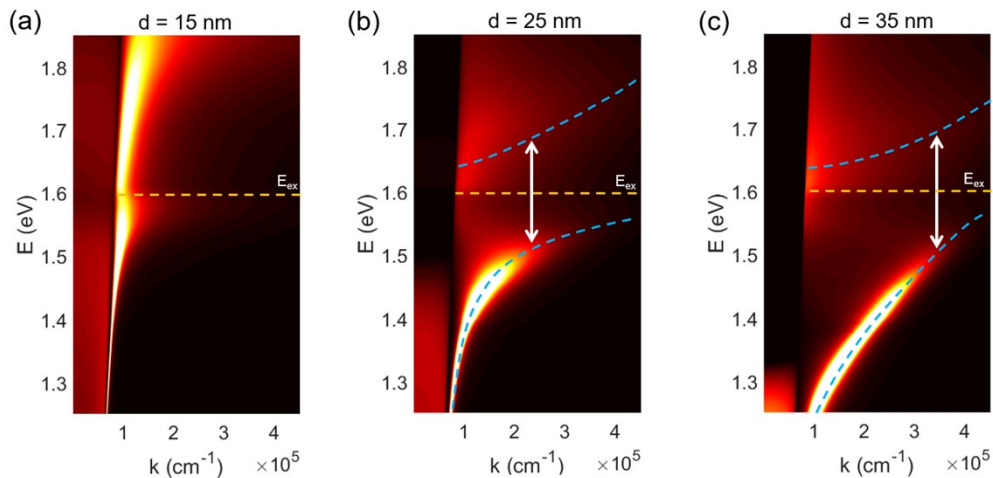
Fig. S7. Dispersion diagrams of the EPP mode at various thicknesses of WSe₂. The blue dashed curves mark the upper and lower branches of exciton-plasmon polaritons, the orange dashed lines mark the exciton energy, and the white arrows mark the Rabi splitting energy.
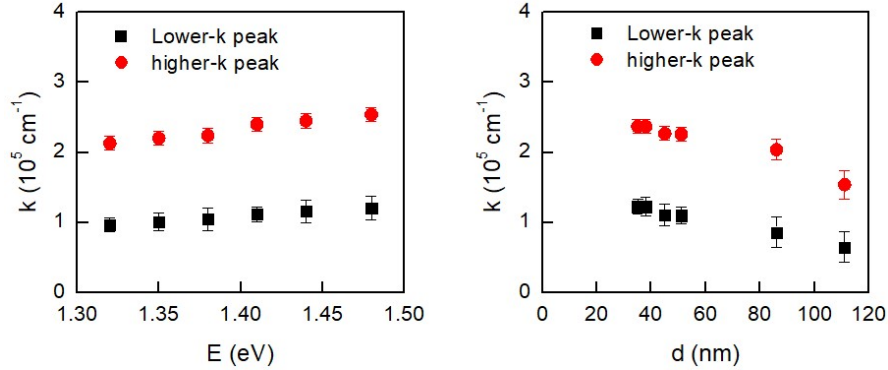

Fig. S8. (a) FT peak location versus excitation energy for both the lower-*k* and higher-*k* peaks. (b) FT peak location versus WSe₂ thickness for both the lower-*k* and higher-*k* peaks.
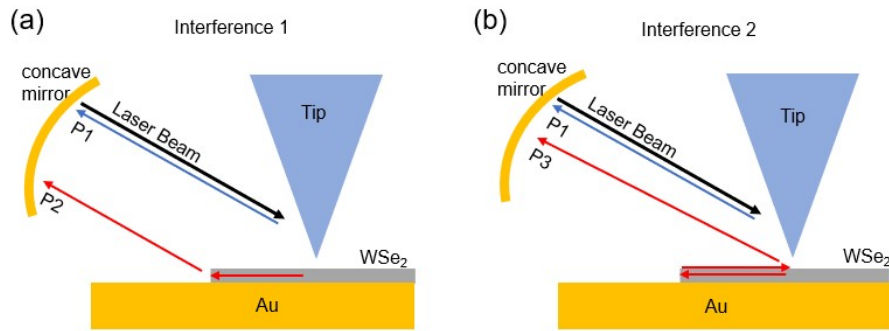

Fig. S9. Sketches of the configurations of beam paths for the two types of interferences.
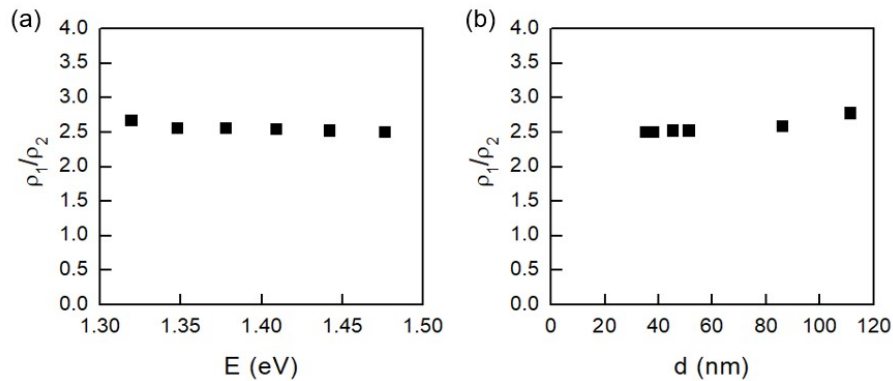

Fig. S10. The ratio of fringe periods from two types of interferences (see Fig. S9) extracted from both energy-dependence and thickness-dependence data.
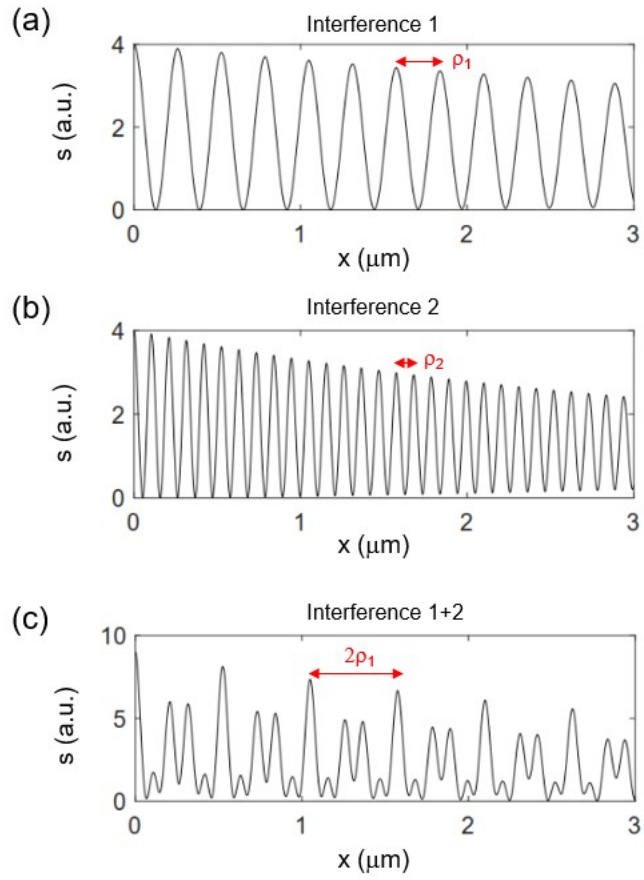
Fig. S11. Simulated periodic fringes generated due to two types of interferences (a,b) and their combination. The arrows mark the periods in these fringes.